



Superconductivity in black phosphorus and the role of dynamical screening

Viktor Christiansson , Francesco Petocchi, and Philipp Werner
 Department of Physics, University of Fribourg, 1700 Fribourg, Switzerland

 (Received 27 January 2022; revised 3 May 2022; accepted 5 May 2022; published 19 May 2022)

Simple cubic phosphorus exhibits superconductivity with a maximum T_c of up to 12 K under pressure. The pressure dependence of T_c cannot be consistently explained with a simple electron-phonon mechanism, which has stimulated investigations into the role of electronic correlations and plasmonic contributions. Here we solve the gap equation of density functional theory for superconductors using different electron-electron and electron-phonon contributions to the kernel. We find that the phonon contribution alone yields an overestimation of T_c , while the addition of the static electronic contribution results in an underestimation. Taking into account the full frequency dependence of the screened interaction, the one-shot GW approximation predicts T_c values in good agreement with the experiments in the pressure range appropriate for the cubic phase. We also explore the use of quasiparticle bands in the calculation of the electronic and phononic kernels, and show that this modification significantly improves T_c in the high-pressure region.

DOI: [10.1103/PhysRevB.105.174513](https://doi.org/10.1103/PhysRevB.105.174513)

I. INTRODUCTION

Black phosphorus at ambient conditions is a layered semiconductor with a narrow gap. It turns into a metallic simple cubic phase at a pressure of about 10 GPa [1], and the cubic structure has been reported to remain stable up to 107 GPa [2]. At low temperatures, superconductivity is observed for pressures above 5 GPa, and the pressure dependence of the superconducting critical temperature T_c has been the subject of numerous experimental and theoretical studies. Despite this effort, a thorough theoretical understanding of the pairing mechanism and superconductivity in cubic phase phosphorus is still lacking. On the experimental side, the situation is further complicated by the wide variation in the measured T_c values, depending on the experimental protocol, as indicated in Fig. 1. For example, it was shown by Kawamura *et al.* [3–5] that the precise pressure-temperature path has significant effects on the pressure dependence of the superconducting critical temperature. With a certain choice of thermodynamical path, they obtained an almost constant T_c with increasing pressure, whereas another path produced a more rapidly increasing T_c . Later experiments by Wittig *et al.* [6] showed a valleylike structure at lower pressures, which agrees with a similar finding by Guo *et al.* in Ref. [7]. The latter results, however, predicted a roughly constant T_c at higher pressures forming a ridgelike structure, whereas the former found a decreasing T_c after a maximum near 23 GPa. Yet another form of the T_c versus pressure curve was reported by Karuzawa *et al.* [8] who measured a pressure dependence with a single maximum of T_c around 32 GPa.

Different mechanisms have been proposed to explain the remarkable robustness of T_c under high pressure and various features in the experimental measurements. However, no consistent theory for the full pressure dependence and for the pairing mechanism has so far emerged. Based on measurements of the Hall coefficient, Guo *et al.* [7] interpreted

the valley structure in the T_c -versus-pressure diagram around 17 GPa as originating from a Lifshitz transition in the simple cubic phase. This has later been supported by the theoretical analysis of Wu *et al.* [10] who performed density functional theory (DFT) [11,12] calculations of the Fermi surface and reported two subsequent Lifshitz transitions occurring in the pressure range where, using the McMillan equation [13,14], a T_c valley was also predicted. Flores-Livas *et al.* [9], using an *ab-initio* calculation based on DFT for superconductors (SCDFT) [15–17] and the static interaction coming from a random-phase approximation (RPA) [18] calculation, also

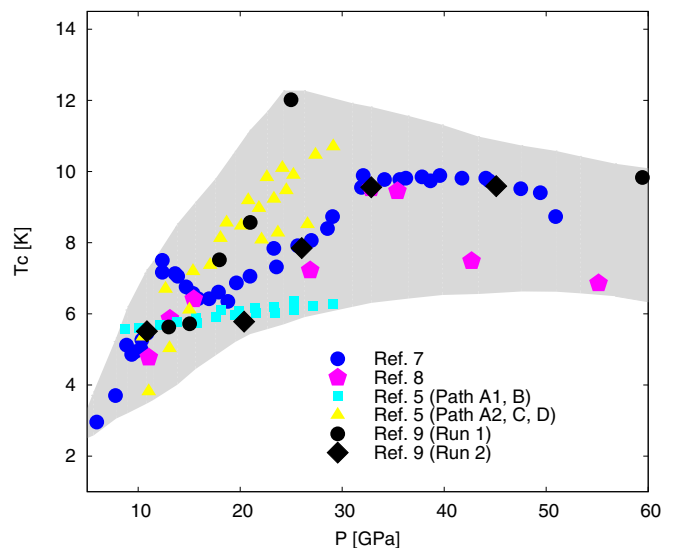


FIG. 1. Pressure dependence of the experimental superconducting critical temperature T_c . The data have been extracted from Refs. [5,7–9], as indicated in the legend. The shaded area outlines the spread of measured values of T_c and will be used to test our theoretical results.

argued that the rapid increase of T_c was due to a Lifshitz transition. These authors furthermore argued that the Lifshitz transition did not occur within the simple cubic phase but rather as a result of a structural transition from the rhombohedral to the simple cubic phase, while Ref. [7] reports a transition to the simple cubic phase around 10–13 GPa. Their analysis further suggested that the discrepancies seen in the experimental results up to 25 GPa can be explained by the coexistence of different structural phases. Neither of the theoretical studies was, however, able to reproduce the plateau found experimentally by Guo *et al.* for pressures between 30 and 50 GPa as well as Flores-Livas *et al.* in their second experimental run. Since the static interaction used in the earlier work by Flores-Livas *et al.* predicted a peak instead of a ridge, Wu *et al.* hypothesized that plasmonic contributions from the inclusion of the full frequency-dependent interaction [19] may provide an additional effective attraction which stabilizes the T_c at higher pressures.

The goal of our study is to go beyond the previous predictions based on the McMillan formula or static RPA interactions by considering also the dynamic (frequency-dependent) contribution to the screened interaction in SCDFT, as proposed by Akashi and Arita in Ref. [19]. Using this *ab-initio* scheme, we will study different levels of approximations to the electron-electron interaction, including RPA, one-shot and self-consistent (sc)GW [20], and GW plus extended dynamical mean-field theory (GW+EDMFT) [21–24]. For better consistency between the calculation of the interaction and the SCDFT scheme used to predict T_c , we furthermore explore a quasiparticle extension of the formalism. In contrast with the previous SCDFT study [9], we assume the simple cubic phase in the whole pressure range, since this is the experimentally observed structure for pressures in the most interesting region of the possible valley-ridge T_c structure.

The paper is organized as follows. In Sec. II we detail the SCDFT formalism and the methods we use to obtain the screened interaction. In Sec. III we present our results and compare them to the available experimental data and earlier theoretical studies, while in Sec. IV we summarize our conclusions.

II. METHOD

A. General remarks

In this section, we introduce the methods we use for predicting T_c within the framework of SCDFT, as well as some computational details. First, the band structure of cubic phase phosphorus obtained from a DFT calculation will be presented in Sec. II B, where we also show the theoretical pressure-volume curve which is used to compare to experiments. In Sec. II C we introduce our seven-band model and the methods used to compute the dynamically screened interactions for it, while the estimation of the phononic contribution is discussed in Sec. II D. In Sec. II E we explain the calculation of T_c by the SCDFT formalism.

B. Band structure for cubic phase phosphorus

All the calculations start with a DFT calculation of the electronic structure of phosphorus in the simple cubic phase. The

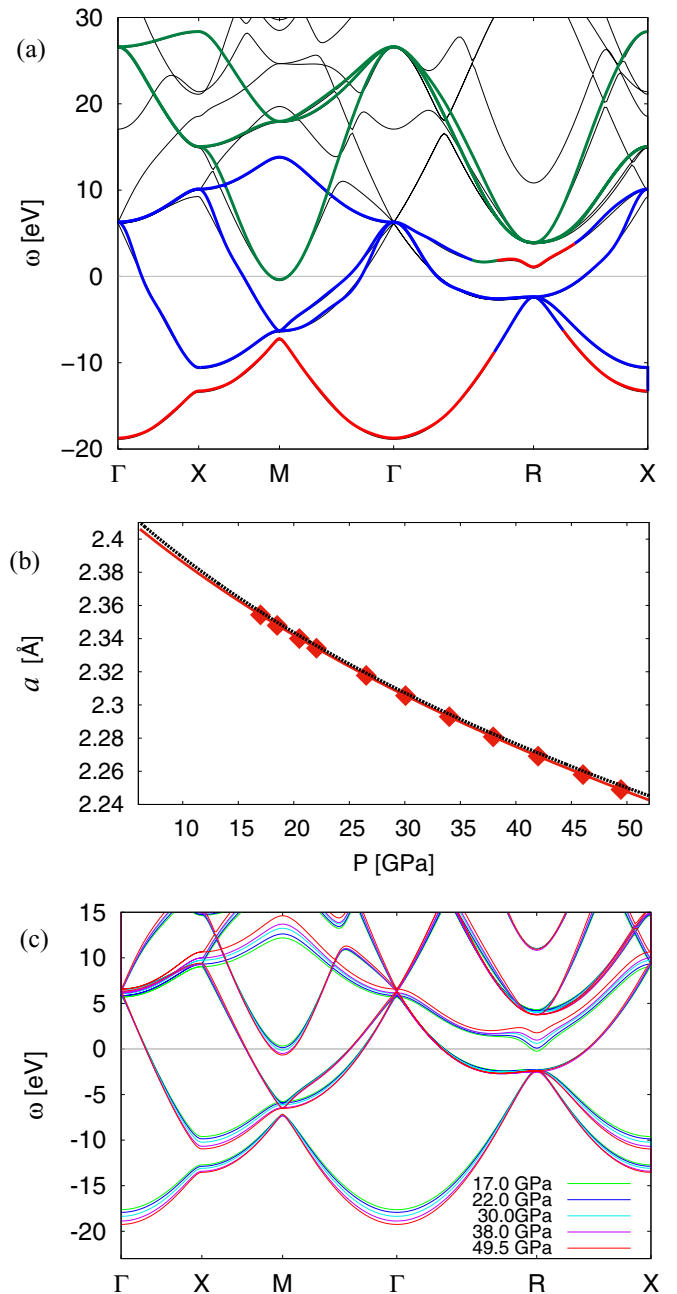


FIG. 2. (a) DFT band structure along high-symmetry lines for simple cubic phosphorus at a pressure of ~ 38 GPa. The colored superimposed lines define the low-energy subspace spanned by seven bands; red, blue, and green indicate majority s -, p -, and t_{2g} -like orbital characters, respectively. (b) Theoretical pressure dependence of the lattice constant a used for the comparison between experimental and theoretical data from FLEUR (red) and ELK (dotted black). The diamonds mark the pressures used for the T_c estimates. (c) Pressure dependence of the band structure.

generalized-gradient approximation (GGA) [25], as implemented in the full-potential linearized augmented plane-wave code FLEUR [26], is used to obtain the *ab-initio* band structure on a $32 \times 32 \times 32$ \mathbf{k} -point grid. The band structure along high-symmetry lines for one pressure ($P \approx 38$ GPa) is shown in Fig. 2(a). The orbital characters of the bands near the Fermi energy are superimposed in Fig. 2(a), showing the dominant

contribution to the bands crossing the Fermi energy to come from orbitals of p character. In agreement with earlier theoretical works [10,27–29], on increasing pressure we observe two consecutive Lifshitz transitions; the first is associated with the disappearance of a pocket of predominantly s character around the R momentum between 21 and 22 GPa, which is followed by a second one between 22 and 23 GPa with a pocket of d character appearing around the M momentum. We show the pressure dependence of the band structure in Fig. 2(c). Additional details on the electronic structure for simple cubic phosphorus under pressure can be found, e.g., in Refs. [10,27–29].

For comparison with the experimental results, we also fit the energy-volume data of the DFT calculations using the Vinet equation of state [30] to obtain the theoretical pressure corresponding to a lattice constant in the simple cubic phase; see Fig. 2(b).

C. Dynamically screened interactions

To move beyond DFT, we define a low-energy model consisting of seven orbitals using maximally localized Wannier functions [31] from the Wannier90 library [32] starting from orbitals of $3s$, p , and t_{2g} character. This provides a low-energy model in good agreement with the DFT band structure in a large energy range around the Fermi energy, as shown in Fig. 2(a). The band character is indicated by the majority contribution of the s -, p -, and t_{2g} -like Wannier orbitals to the model bands. The Wannier spreads for these orbitals are 1.048, 1.500, and 1.399 Å², respectively. We have checked that additionally including states of e_g character in a nine-band model does not significantly change the description around the Fermi energy.

We subsequently perform a systematic downfolding of the full band structure to the low-energy space by means of a constrained RPA (cRPA) [33] and a one-shot GW calculation [20]. In the GW approximation [20], the self-energy is expanded to first order in the screened Coulomb interaction W , which produces a set of coupled equations for the Green's function G , self-energy Σ , screened interaction W , and polarization Π .

In reciprocal space and at zero temperature the self-energy is given by

$$\Sigma_{\mathbf{k}}(\omega) = \frac{i}{2\pi} \sum_{\mathbf{q}} \int d\omega' G_{\mathbf{k}-\mathbf{q}}(\omega + \omega') W_{\mathbf{q}}(\omega'). \quad (1)$$

The screened interaction $W_{\mathbf{q}}$ is calculated by screening the bare Coulomb interaction $v_{\mathbf{q}}$ by the polarization function $\Pi_{\mathbf{q}}$,

$$W_{\mathbf{q}}(\omega) = v_{\mathbf{q}} + v_{\mathbf{q}} \Pi_{\mathbf{q}}(\omega) W_{\mathbf{q}}(\omega), \quad (2)$$

where $\Pi_{\mathbf{q}}$ is calculated within RPA as

$$\Pi_{\mathbf{q}}(\omega) = -\frac{i}{2\pi} \sum_{\mathbf{k}} \int d\omega' G_{\mathbf{k}}(\omega') G_{\mathbf{k}-\mathbf{q}}(\omega' - \omega). \quad (3)$$

The GW approximation requires as initial input a noninteracting Green's function, $G_{\mathbf{k}}^0$, which is commonly taken from a DFT calculation. This replaces initially $G_{\mathbf{k}}$ in Eqs. (1)–(3), which yield the Green's function of the one-shot GW (or

G^0W^0) approximation,

$$G_{\mathbf{k}}^{-1}(\omega) = (G_{\mathbf{k}}^0)^{-1}(\omega) - \Sigma_{\mathbf{k}}(\omega). \quad (4)$$

Starting from the DFT-derived $G_{\mathbf{k}}^0$, Eqs. (1)–(4) can be iterated by using the updated Green's function G in the next iteration, and if this is repeated until self-consistency, the method is referred to as $scGW$. In practice, however, good or even better results are obtained by one-shot GW in many cases, unless the self-consistency loop is modified [34].

Through a G^0W^0 calculation in the full space, using the disentangled band structure [35], we obtain the embedding self-energy for the seven bands of our model, $\Sigma_{\mathbf{k}}^{\text{embedding}}(\omega)$ which, together with $G_{\mathbf{k}}^0$, yields the effective bare propagators in the model subspace [23,24]. Similarly, the cRPA method is used to calculate the effective bare interaction within the model space; the bands inside the low-energy subspace, in our case the seven-band model, are excluded from the polarization in the G^0W^0 calculation [Eq. (3)]. An equation similar to Eq. (2) is then obtained for the partially screened interaction

$$U_{\mathbf{q}}(\omega) = v_{\mathbf{q}} + v_{\mathbf{q}} \Pi_{\mathbf{q}}^r(\omega) U_{\mathbf{q}}(\omega), \quad (5)$$

where the superscript r indicates that the summations in the formula for the RPA polarization should be done over all bands except for transitions within the model subspace. The resulting frequency-dependent interaction $U_{\mathbf{q}}(\omega)$ represents the effective bare interaction for the model space. By subsequently screening $U_{\mathbf{q}}$ with the polarization $\Pi_{\mathbf{q}}^{\text{model}}$ from the previously excluded bands that define the model subspace, the fully screened interaction $W_{\mathbf{q}}$ in Eq. (2) is recovered.

The G^0W^0 and cRPA calculations were performed with the SPEX code [36] at zero temperature. A $8 \times 8 \times 8$ \mathbf{k} grid was used and DFT bands up to 100 eV were included in the calculation for both the polarization function and the self-energy. Having obtained the effective bare propagators $G_{\mathbf{k}}^0$ and interactions $U_{\mathbf{q}}$ in the model space, we employed several approximate methods to compute the screened interaction needed for the SCDF formalism (see Sec. II E). These will be briefly explained in the following.

For the RPA and GW variants of the screened interaction, we have evaluated $W_{\mathbf{q}}$ in Eq. (2) using the RPA-type polarization function [Eq. (3)] with the following choices of $G_{\mathbf{k}}$ and interaction parameters:

(1) The DFT noninteracting Green's function, rotated from the Kohn-Sham basis to the Wannier basis, and the bare interaction $v_{\mathbf{q}}$. This defines W^{RPA} .

(2) The bare effective propagator in the model space obtained with Eq. (4) using the DFT $G_{\mathbf{k}}^0$ and $\Sigma_{\mathbf{k}}^{\text{embedding}}$ from the G^0W^0 calculation. Furthermore, $v_{\mathbf{q}}$ is replaced by the partially screened interaction $U_{\mathbf{q}}(\omega)$. This procedure defines $W^{G^0W^0}$.

(3) Similar to point 2, but with the Green's function obtained in a self-consistent manner from the finite-temperature equivalents of Eqs. (1)–(4) (see, e.g., Ref. [24]) within the model subspace. Again, $U_{\mathbf{q}}(i\omega_n)$ replaces $v_{\mathbf{q}}$ as the bare interaction in Eq. (2). This calculation defines W^{scGW} .

The full expression for the Green's function in method 3 is

$$G_{\mathbf{k}}^{-1} = i\omega_n + \mu - \varepsilon_{\mathbf{k}}^{\text{DFT}} + V_{\mathbf{k}}^{\text{XC}} - (\Sigma_{\mathbf{k}}^{G^0W^0} - \Sigma_{\mathbf{k}}^{G^0W^0}|_{\text{model}} + \Sigma_{\mathbf{k}}^{\text{scGW}}|_{\text{model}}). \quad (6)$$

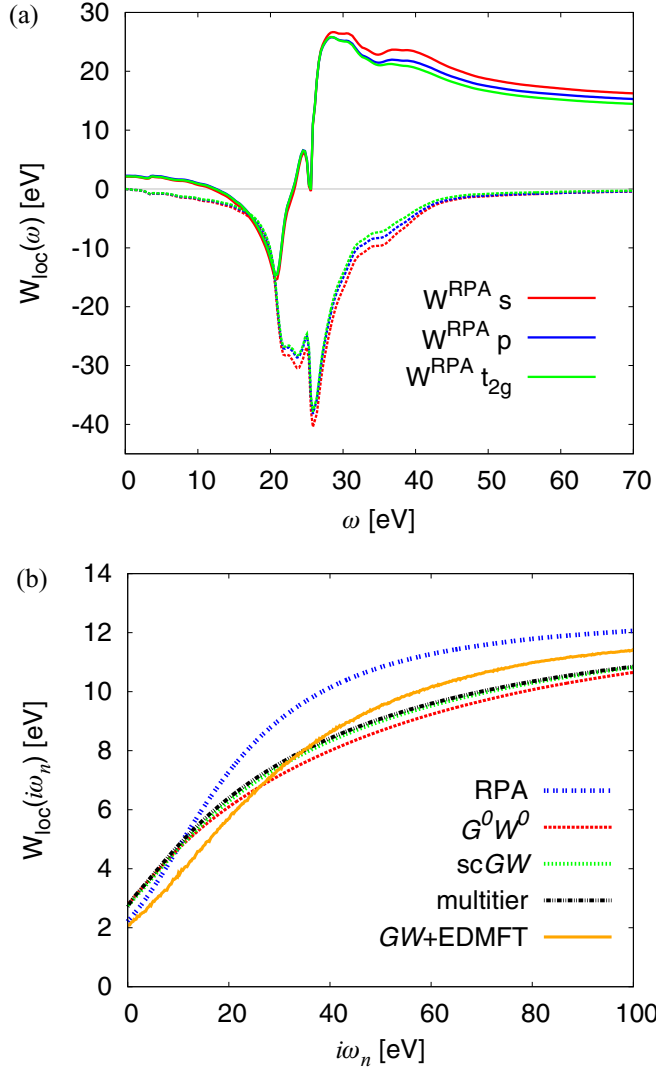


FIG. 3. (a) Frequency dependence of the fully screened local interaction, $W_{\text{loc}}(\omega)$, calculated within RPA on the real axis. The full and dashed lines show the real and imaginary parts for the orbitals with s (red), p (blue), and t_{2g} character (green). (b) Comparison of the local fully screened interaction on the Matsubara axis for the orbital with t_{2g} character calculated within RPA (blue), G^0W^0 (red), scGW (green), multiter GW+EDMFT (black), and GW+EDMFT (orange).

The G^0W^0 calculation provides the contribution from the states outside the model, with the exchange-correlation potential $V_{\mathbf{k}}^{\text{XC}}$ from the DFT calculation and the self-energy from a one-shot G^0W^0 calculation within the model space ($\Sigma_{\mathbf{k}}^{G^0W^0}|_{\text{model}}$) removed to avoid double countings of interaction contributions [23,24].

In addition we have calculated the screened interaction obtained from a fully self-consistent GW+EDMFT simulation [21,23,24] ($W^{GW+EDMFT}$) where we update all seven orbitals with the local vertex corrections from EDMFT [37–39] and in a multiter GW+EDMFT simulation, where we limit the EDMFT corrections to only the t_{2g} -like orbitals (W^{multiter}) [24].

We perform the GW+EDMFT and scGW calculations at nonzero temperatures by first analytically continuing the

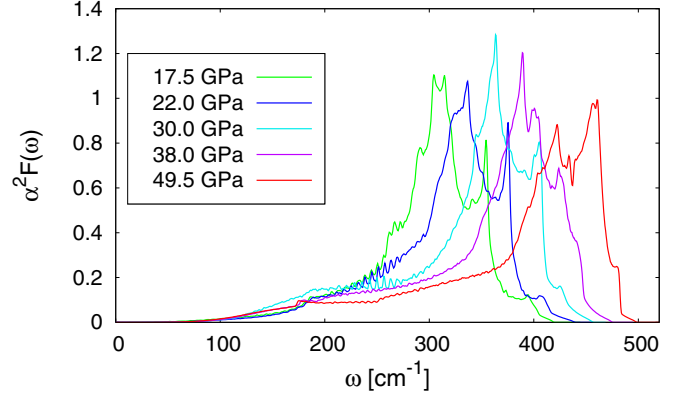


FIG. 4. The Eliashberg function $\alpha^2F(\omega)$ for simple cubic phosphorus at several pressures used in this work.

initial zero-temperature calculations to the Matsubara axis. Due to the large computational cost associated with these non-local, frequency-dependent calculations, we are here limited to a relatively high temperature of $T \approx 380$ K (inverse temperature $\beta = 30$ eV $^{-1}$). We have checked that the screened interactions obtained in this way do not display significant changes when the temperature is further lowered, so that we use them as an approximation also for the low-temperature system.

In Fig. 3(b) we show the t_{2g} -like component of the interaction from the different methods. The SCDFT formalism requires the interaction on the Matsubara axis, but for comparison we also show in Fig. 3(a) the real-frequency dependence of the local W^{RPA} which we can obtain directly from the G^0W^0 downfolding without analytical continuation. This figure displays the RPA interactions for the s -, p -, and t_{2g} -like components, which are very similar. For the calculation of T_c in Sec. II E we retain all the off-diagonal components of W . The method employed in this work does not allow us to directly identify the relative importance of the contributions from the different bands.

D. Eliashberg function

The phononic contribution to the superconductivity enters the SCDFT formalism used in this work via the Eliashberg function [40] which is calculated as

$$\alpha^2F(\omega) = \frac{1}{N(0)} \sum_{\lambda, \mathbf{q}} \sum_{n, n', \mathbf{k}} |g_{\lambda, \mathbf{q}}^{n\mathbf{k}, n'(\mathbf{k}+\mathbf{q})}|^2 \times \delta(\varepsilon_{n\mathbf{k}}) \delta(\varepsilon_{n'\mathbf{k}+\mathbf{q}}) \delta(\omega - \omega_{\lambda\mathbf{q}}). \quad (7)$$

Here $\varepsilon_{n\mathbf{k}}$ denotes the one-particle energies (measured from the Fermi energy) for the states (n, \mathbf{k}) obtained from the DFT band structure, the phonon frequencies are $\omega_{\lambda\mathbf{q}}$ for wave-vector \mathbf{q} and mode λ , and $N(0)$ is the density of states (DOS) at the Fermi energy. The matrix elements of the electron-phonon coupling constants are given by

$$g_{\lambda, \mathbf{q}}^{n\mathbf{k}, n'(\mathbf{k}+\mathbf{q})} = \frac{1}{\sqrt{2M\omega_{\lambda\mathbf{q}}}} \langle n', (\mathbf{k} + \mathbf{q}) | \delta_{\mathbf{q}}^{\lambda} V^{\text{KS}} | n, \mathbf{k} \rangle, \quad (8)$$

where the variation of the Kohn-Sham potential with respect to the displacements is denoted by $\delta_{\mathbf{q}}^{\lambda} V^{\text{KS}}$, and M is the mass of the atom. In Fig. 4 we show $\alpha^2F(\omega)$ at several pressures

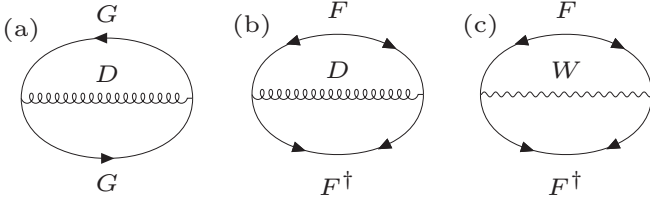


FIG. 5. Diagrammatic representation of the exchange-correlation kernels used in this work; (a) and (b) show the electron-phonon contributions to \mathcal{Z}^{ph} and \mathcal{K}^{ph} , respectively, while (c) illustrates the electron-electron contribution to \mathcal{K}^{el} (the kernels are defined in the text). The curled line represents the phonon propagator D , the wavy line represents the screened Coulomb interaction W , the single-arrowed lines the electronic Green's function G , and the double-arrowed lines represent the anomalous Green's functions F and F^\dagger .

used in this work. A more detailed discussion of the pressure dependence of the phonons for simple cubic phosphorus can be found, e.g., in Refs. [9,10,29].

The phononic contributions were calculated with the supercell method as implemented in the ELK code [41] using the GGA functional on a $8 \times 8 \times 8$ \mathbf{q} grid and a $32 \times 32 \times 32$ \mathbf{k} grid. The interpolated fine grids used for the \mathbf{k} and \mathbf{q} integrations in Eq. (7) were taken to be $128 \times 128 \times 128$ and $200 \times 200 \times 200$, respectively, which was sufficient for good convergence. Since the volume-pressure curve is in good agreement between FLEUR and ELK, as shown in Fig. 2(b), and as both are full-potential all-electron codes, the electronic and phononic contributions to the SCDFT calculations described in the next section should be compatible.

E. SCDFT

SCDFT [15–17] is a formalism which allows to predict the superconducting critical temperature T_c from first principles. The T_c is estimated from the vanishing of the gap function $\Delta_{n\mathbf{k}}$, which is obtained as the self-consistent solution of the gap equation

$$\Delta_{n\mathbf{k}} = -\mathcal{Z}_{n\mathbf{k}} \Delta_{n\mathbf{k}} - \frac{1}{2} \sum_{n'\mathbf{k}'} \mathcal{K}_{n\mathbf{k},n'\mathbf{k}'} \frac{\tanh[(\beta/2)E_{n'\mathbf{k}'}]}{E_{n'\mathbf{k}'}} \Delta_{n'\mathbf{k}'}. \quad (9)$$

This equation involves the exchange-correlation kernels \mathcal{Z} and \mathcal{K} , the energies $E_{n\mathbf{k}} = \sqrt{\varepsilon_{n\mathbf{k}}^2 + \Delta_{n\mathbf{k}}^2}$, and the inverse temperature β . In this study, the diagonal \mathcal{Z} term is assumed to consist of only the electron-phonon contribution $\mathcal{Z} = \mathcal{Z}^{\text{ph}}$, whereas for the \mathcal{K} kernel we include both the electron-phonon and the electron-electron contributions $\mathcal{K} = \mathcal{K}^{\text{ph}} + \mathcal{K}^{\text{el}}$. A diagrammatic representation of the exchange-correlation functionals is shown in Fig. 5.

Within the \mathbf{k} -dependent formalism derived in Ref. [16], the expressions for the electron-phonon kernels are

$$\mathcal{Z}_{n\mathbf{k}}^{\text{ph}} = \frac{1}{\tanh[(\beta/2)\varepsilon_{n\mathbf{k}}]} \sum_{n'\mathbf{k}'} \sum_{\lambda\mathbf{q}} |g_{\lambda\mathbf{q}}^{n\mathbf{k},n'\mathbf{k}'}|^2 \times [J(\varepsilon_{n\mathbf{k}}, \varepsilon_{n'\mathbf{k}'}, \omega_{\lambda\mathbf{q}}) + J(\varepsilon_{n\mathbf{k}}, -\varepsilon_{n'\mathbf{k}'}, \omega_{\lambda\mathbf{q}})] \quad (10)$$

and

$$\mathcal{K}_{n\mathbf{k},n'\mathbf{k}'}^{\text{ph}} = \frac{1}{\tanh[(\beta/2)\varepsilon_{n\mathbf{k}}]} \frac{1}{\tanh[(\beta/2)\varepsilon_{n'\mathbf{k}'}]} \sum_{\lambda\mathbf{q}} |g_{\lambda\mathbf{q}}^{n\mathbf{k},n'\mathbf{k}'}|^2 \times [I(\varepsilon_{n\mathbf{k}}, \varepsilon_{n'\mathbf{k}'}, \omega_{\lambda\mathbf{q}}) - I(\varepsilon_{n\mathbf{k}}, -\varepsilon_{n'\mathbf{k}'}, \omega_{\lambda\mathbf{q}})], \quad (11)$$

with the functions I and J defined in terms of the Fermi-Dirac ($n_F(\varepsilon)$) and Bose-Einstein ($n_B(\omega)$) distributions as

$$I(\varepsilon, \varepsilon', \omega) = n_F(\varepsilon)n_F(\varepsilon')n_B(\omega) \times \left(\frac{e^{\beta\varepsilon} - e^{\beta(\varepsilon'+\omega)}}{\varepsilon - \varepsilon' - \omega} - \frac{e^{\beta\varepsilon'} - e^{\beta(\varepsilon+\omega)}}{\varepsilon - \varepsilon' + \omega} \right), \quad (12)$$

$$J(\varepsilon, \varepsilon', \omega) = \tilde{J}(\varepsilon, \varepsilon', \omega) - \tilde{J}(\varepsilon, \varepsilon', -\omega), \quad (13)$$

$$\tilde{J}(\varepsilon, \varepsilon', \omega) = -\frac{n_F(\varepsilon) + n_B(\omega)}{\varepsilon - \varepsilon' - \omega} \left(\frac{n_F(\varepsilon') - n_F(\varepsilon - \omega)}{\varepsilon - \varepsilon' - \omega} - \beta n_F(\varepsilon - \omega)n_F(-\varepsilon + \omega) \right). \quad (14)$$

For the electronic contribution to the \mathcal{K} kernel, we employ the fully frequency-dependent interaction kernel proposed in Ref. [19], which has been shown in previous studies to properly account for the electron-electron interaction effects. This term is separated into the static and dynamic contributions, $\mathcal{K}^{\text{el}} = \mathcal{K}^{\text{el, static}} + \mathcal{K}^{\text{el, dynamic}}$, to identify their respective effects. The static part of the kernel is given by the static screened interaction

$$\mathcal{K}_{n\mathbf{k},n'\mathbf{k}'}^{\text{el, static}} = W_{n\mathbf{k},n'\mathbf{k}'}(0), \quad (15)$$

and the dynamic (frequency-dependent) part by

$$\mathcal{K}_{n\mathbf{k},n'\mathbf{k}'}^{\text{el, dyn}} = \lim_{\Delta_{n\mathbf{k}} \rightarrow 0} \frac{1}{\tanh[(\beta/2)E_{n\mathbf{k}}]} \frac{1}{\tanh[(\beta/2)E_{n'\mathbf{k}'}]} \times \frac{1}{\beta^2} \sum_{\omega_1 \omega_2} F_{n\mathbf{k}}(i\omega_1) F_{n'\mathbf{k}'}(i\omega_2) [W_{n\mathbf{k},n'\mathbf{k}'}^{\text{dyn}}(i\omega_1 - i\omega_2)]. \quad (16)$$

The anomalous (electronic) Green's function $F_{n\mathbf{k}}$ is given by

$$F_{n\mathbf{k}}(i\omega_j) = \frac{1}{i\omega_j + E_{n\mathbf{k}}} - \frac{1}{i\omega_j - E_{n\mathbf{k}}}, \quad (17)$$

where the ω_j are fermionic Matsubara frequencies, and for simplicity we have introduced the notation $W_{n\mathbf{k},n'\mathbf{k}'}^{\text{dyn}}(i\omega_1 - i\omega_2) = W_{n\mathbf{k},n'\mathbf{k}'}(i\omega_1 - i\omega_2) - W_{n\mathbf{k},n'\mathbf{k}'}(0)$. This can be simplified [42] using the variable transformation $i\nu = i(\omega_1 - \omega_2)$ to the following expression which only requires a summation over a single bosonic frequency ν ,

$$\mathcal{K}_{n\mathbf{k},n'\mathbf{k}'}^{\text{el, dyn}} = \lim_{\Delta_{n\mathbf{k}} \rightarrow 0} \frac{1}{\tanh[(\beta/2)E_{n\mathbf{k}}]} \frac{1}{\tanh[(\beta/2)E_{n'\mathbf{k}'}]} \frac{1}{\beta} \times \sum_{\nu} [W_{n\mathbf{k},n'\mathbf{k}'}^{\text{dyn}}(i\nu)] \times \left(\frac{2(E_{n\mathbf{k}} - E_{n'\mathbf{k}'})}{(E_{n\mathbf{k}} - E_{n'\mathbf{k}'})^2 + \nu^2} (n_F(E_{n\mathbf{k}}) - n_F(E_{n'\mathbf{k}'})) + \frac{2(E_{n\mathbf{k}} + E_{n'\mathbf{k}'})}{(E_{n\mathbf{k}} + E_{n'\mathbf{k}'})^2 + \nu^2} (n_F(-E_{n\mathbf{k}}) - n_F(E_{n'\mathbf{k}'})) \right). \quad (18)$$

The screened interaction W has commonly been computed using RPA or the adiabatic local density approximation [43,44], whereas in the present study we will compare the results for the screened interactions obtained by the different diagrammatic schemes described in Sec. II C.

The phononic contribution requires a sufficiently dense \mathbf{k} grid close to the Fermi energy for convergence in the low-energy regime. Often this is handled by a random sampling method with a higher density of \mathbf{k} points close to the Fermi energy to ensure a sufficient resolution [17,45]. Due to the prohibitively large computational cost for scGW and GW+EDMFT, which scales quadratically with the number of \mathbf{k} points, we are unable to calculate $W_{n\mathbf{k},n'\mathbf{k}'}$ directly in this way and instead would have to interpolate from a coarse grid. For this reason, we resorted to the energy-averaged formalism [17] where the electron-electron interaction is first evaluated using the *ab-initio* methods on a coarse grid, as described in Section II C. We thereafter obtain the kernels by averaging over isoenergetic surfaces using analytical expressions for the phononic parts while the electronic kernel has to be obtained numerically.

The energy-averaged version of the gap equation takes the form [17]

$$\Delta(\varepsilon) = -\mathcal{Z}(\varepsilon)\Delta(\varepsilon) - \frac{1}{2} \int_{-\mu}^{\infty} d\varepsilon' N(\varepsilon') \mathcal{K}(\varepsilon, \varepsilon') \frac{\tanh[(\beta/2)E']}{E'} \Delta(\varepsilon'), \quad (19)$$

and the energy-averaged phononic kernel \mathcal{Z}^{ph} becomes

$$\mathcal{Z}^{\text{ph}}(\varepsilon) = -\frac{1}{\tanh[(\beta/2)\varepsilon]} \int_{-\mu}^{\infty} d\varepsilon' \times \int d\omega \alpha^2 F(\omega) [J(\varepsilon, \varepsilon', \omega) + J(\varepsilon, -\varepsilon', \omega)], \quad (20)$$

where μ is the chemical potential, and the Eliashberg function, $\alpha F(\omega)$, has been defined in Sec. II D. As previously noted, the \mathcal{K} kernel consists of two parts in our calculations: The electron-phonon (\mathcal{K}^{ph}) and the electron-electron (\mathcal{K}^{el}) contributions. The electron-phonon kernel within the energy-averaged formalism is expressed as

$$\mathcal{K}^{\text{ph}}(\varepsilon, \varepsilon') = \frac{2}{\tanh[(\beta/2)\varepsilon] \tanh[(\beta/2)\varepsilon']} \frac{1}{N(0)} \times \int d\omega \alpha^2 F(\omega) [I(\varepsilon, \varepsilon', \omega) - I(\varepsilon, -\varepsilon', \omega)], \quad (21)$$

with $N(\varepsilon)$ the DOS, whereas the integrals over the isoenergetic surfaces must be done numerically for the electron-electron contribution,

$$\mathcal{K}^{\text{el}}(\varepsilon, \varepsilon') = \frac{1}{N(\varepsilon)N(\varepsilon')} \sum_{n\mathbf{k},n'\mathbf{k}'} \delta(\varepsilon - \varepsilon_{n\mathbf{k}}) \delta(\varepsilon' - \varepsilon_{n'\mathbf{k}'}) \mathcal{K}_{n\mathbf{k},n'\mathbf{k}'}^{\text{el}}. \quad (22)$$

The final expressions used in this work are

$$\mathcal{K}^{\text{el, static}}(\varepsilon, \varepsilon') = \frac{1}{N(\varepsilon)N(\varepsilon')} \sum_{n\mathbf{k},n'\mathbf{k}'} \delta(\varepsilon - \varepsilon_{n\mathbf{k}}) \delta(\varepsilon' - \varepsilon_{n'\mathbf{k}'}) W_{n\mathbf{k},n'\mathbf{k}'}(0), \quad (23)$$

$$\mathcal{K}^{\text{el, dyn}}(\varepsilon, \varepsilon') = \frac{1}{\tanh[(\beta/2)\varepsilon]} \frac{1}{\tanh[(\beta/2)\varepsilon']} \frac{1}{\beta} \sum_{\nu} \left[\frac{1}{N(\varepsilon)N(\varepsilon')} \sum_{n\mathbf{k},n'\mathbf{k}'} \delta(\varepsilon - \varepsilon_{n\mathbf{k}}) \delta(\varepsilon' - \varepsilon_{n'\mathbf{k}'}) W_{n\mathbf{k},n'\mathbf{k}'}^{\text{dyn}}(i\nu) \right] \times \left(\frac{2(\varepsilon - \varepsilon')}{(\varepsilon - \varepsilon')^2 + \nu^2} (n_F(\varepsilon) - n_F(\varepsilon')) + \frac{2(\varepsilon + \varepsilon')}{(\varepsilon + \varepsilon')^2 + \nu^2} (n_F(-\varepsilon) - n_F(\varepsilon')) \right), \quad (24)$$

where we made use of the tetrahedron method [46,47] to carry out the \mathbf{k} integrations numerically.

The methods used to compute W at nonzero temperatures are limited to high temperatures (described in Sec. II C) compared with the observed T_c . We assume that the same W can be used for all T_c estimates. Noting that W is an even function in ν , to perform the frequency summation, we replace [48] $\sum_{\nu} \rightarrow \frac{\beta}{\pi} (\int_0^{\nu_{\text{max}}} d\nu + \int_{\nu_{\text{max}}}^{\infty} d\nu)$ and introduce a frequency cutoff $\nu_{\text{max}} = 300$ eV, after which the tail of the interaction is assumed to be constant. This can be justified by checking that the high-energy behavior has approximately reached the bare value. The second integral can then be evaluated analytically and contributes

$$[W^{\text{dyn}}(\nu_{\text{max}})] \left(1 - \frac{2}{\pi} \arctan \left[\frac{\nu_{\text{max}}}{(\varepsilon \pm \varepsilon')} \right] \right) (n_F(\mp\varepsilon) - n_F(\varepsilon'))$$

to the kernel. The remaining integral up to the cutoff is treated numerically using the change of variables $\nu = (\varepsilon \pm \varepsilon')(1 + y)/(1 - y)$ [49].

III. RESULTS

A. General remarks

We computed the critical temperatures from the vanishing of the superconducting gap in Eq. (19) at pressures ranging from ~ 17 to 50 GPa. For pressures below 17 GPa we obtained significant imaginary phonon frequencies around the R momentum, indicative of a structural instability, in agreement with previous DFT calculations for simple cubic phosphorus in this pressure range [10,29]. The weight of these unstable phonon modes rapidly decreases with increasing pressure above 17 GPa and essentially vanishes around 20.5 GPa. We indicate the region with a potential influence from unstable phonon modes by the vertical black line in the P - T_c plots. However, since the weight of the unstable modes is very small in the considered pressure range, we have neglected their contribution in the SCDFT calculations.

To investigate effects related to the method used to obtain the interaction W entering the electron-electron

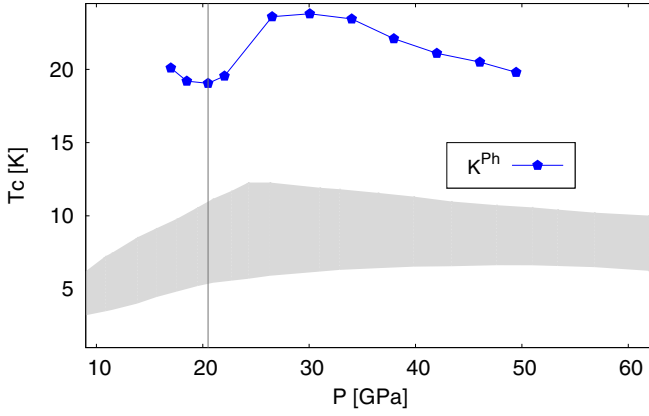


FIG. 6. Theoretically calculated critical temperature T_c with only the phonon kernels as a function of pressure P and compared with the experimental results (gray shading). To the left of the vertical line we observe a structural instability in our phonon calculations.

contribution, we evaluated the pressure dependence of T_c using the methods listed in Sec. II C for both the static and fully dynamic \mathcal{K}^{el} kernels. The results will be presented in order of increasing complexity in the kernels considered starting from a purely phononic kernel and then describing the effects of further including the static electronic part, followed by the simulations with the fully dynamic kernel. Finally we explore a strategy that allows to include the correlation effects not only through the interaction but also through the phononic contribution by replacing the noninteracting band structure used in SCDFT with the quasiparticle band structure.

B. Phonon contribution only

The pressure dependence of the T_c values obtained with only the phonon contributions is shown in Fig. 6. The phonon-only approximation severely overestimates T_c by more than a factor of two compared with the experimental values. This is because such a calculation misses cancellation effects between the phononic and the electronic contributions, which are known to suppress T_c [17]. In more phenomenological theories this problem is usually addressed by introducing effective parameters, for example, in the McMillan equation through the effective interaction parameter μ^* [13,14]. Within the SCDFT formalism employed here, a similar effect is produced by adding the contribution from the static electronic kernel, $\mathcal{K}^{\text{el, static}}$, which drastically reduces the predicted T_c . This underestimation in turn is to a varying extent mitigated by including the contributions from the dynamical kernel, as will be discussed in the following.

C. Phonon contribution plus static electronic contribution

Considering only the static interaction in the calculation of the electronic kernel, $\mathcal{K}^{\text{el}} = \mathcal{K}^{\text{el, static}}$, we obtain a severe underestimation of the critical temperature for all methods employed in this work, as shown in Fig. 7 by the dashed lines. The static results from one-shot GW , $scGW$, and multiter $GW+EDMFT$ are in very close agreement and only one

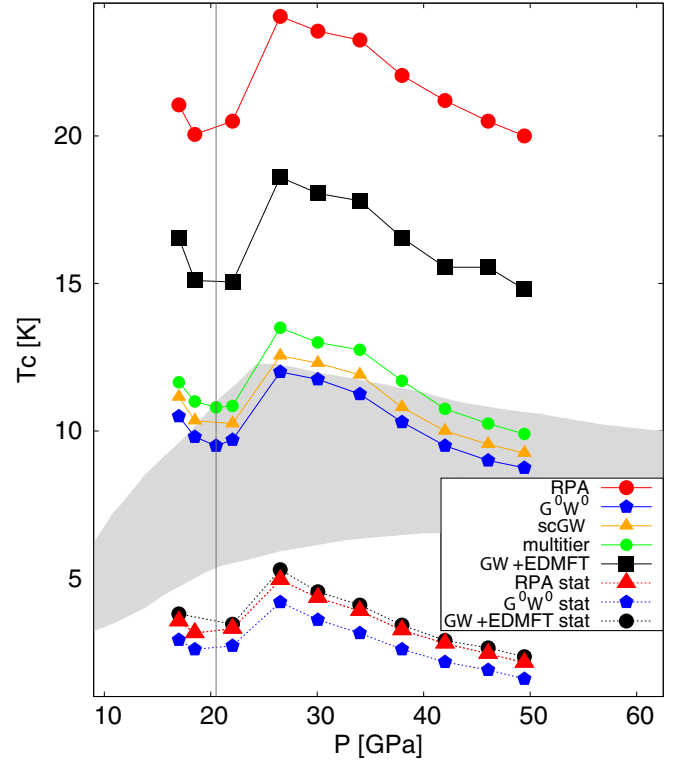


FIG. 7. Theoretically calculated critical temperature T_c as a function of pressure P compared with the experimental results (gray shading). To the left of the vertical line we observe a structural instability in our phonon calculations. Dashed lines show results obtained with the phononic plus static electronic kernels, and the full lines show the results that additionally include the dynamical contribution, i.e., which consider the full frequency dependence of the electronic contributions.

representative pressure- T_c curve is shown for these (labeled G^0W^0 stat).

The predicted T_c from $GW+EDMFT$ and RPA is slightly higher but still severely underestimated compared with the experimental measurements. This is a first indication that adding the local EDMFT corrections to the s - and p -like orbitals produces significant differences compared with the other GW -based schemes, a result which will be discussed further in the following sections. Within the current approach, the different results can be understood from the behavior of the static value of the local screened interaction presented in Fig. 3; the low-frequency screening turns out to be more pronounced for the $GW+EDMFT$ and RPA methods, leading to a larger reduction of the static electron-electron interaction. Since $\mathcal{K}^{\text{el, static}}$ is a positive and approximately constant quantity, it partly cancels the T_c enhancing contributions from the oppositely signed \mathcal{K}^{ph} close to the Fermi energy, which in turn produces the observed differences in the suppression of T_c .

Let us compare these results to phenomenological theories predicting a T_c valley in this region [10]. When only considering the static electronic kernel in our scheme, the static value of the nonlocal, orbital-dependent interaction plays the role of an effective parameter controlling the critical temperature and its pressure dependence. Instead of using it as an adjustable

parameter, however, it is calculated here in a fully *ab-initio* way using a range of methods. All the used methods predict the formation of a valley structure around 20 GPa in the simple cubic phase, a few GPa above the value where such a structure has been observed in experiments [6,7] although at severely underestimated T_c values. Flores-Livas *et al.* [9] also predicted a small valley in this region, although their calculations were in the A7 phase instead of the simple cubic phase in this pressure range.

The fact that our calculated values of T_c consistently underestimate the experimental values irrespective of the method demonstrates the importance of including the dynamic kernel and hence the retardation effect from single-particle and collective charge excitations (plasmons) [19] for an accurate description of the critical temperature.

D. Phonon contribution plus static and dynamic electronic contributions

Within our formalism, the inclusion of the fully dynamical electronic contribution enhances T_c and brings the calculated results into the range of the experimentally measured values, see the symbols connected by full lines in Fig. 7. In addition, compared with the static case, the T_c curves differ more between the methods with an almost rigid shift between the results for one-shot GW , $scGW$, and multiter $GW+EDMFT$. This demonstrates the sensitivity of the SCDFT approach on the dynamic contribution to the electronic kernel and allows us to identify the most suitable method for the present system. The best agreement with experiment is found for one-shot GW . This is consistent with other studies on weakly correlated systems where fully $scGW$ is found to perform worse than one-shot GW [50].

As discussed in the previous section, the static value of W is almost the same for one-shot GW , $scGW$, and multiter $GW+EDMFT$. Instead, we can relate the observed differences to the frequency dependence of the local screened interaction shown in Fig. 3, where the dynamical screening varies more widely between the methods. The significantly reduced RPA screening at higher energies (compared with one-shot GW) together with the overscreened static interaction is responsible for the overestimation of the T_c in this approximation (see the full red line in Fig. 7). Also the $GW+EDMFT$ interaction shows two frequency regimes; at low frequencies, it over-estimates the screening compared with one-shot GW while at high energies, it underestimates it. The net result is again a less accurate T_c (black line in Fig. 7). It should also be noted that, unlike the static kernel, the dynamic one is no longer approximately constant as a function of energy due to the additional factors in Eq. (24). This limits us from drawing any conclusions based on the local interaction only.

The fact that $GW+EDMFT$ worsens the agreement with experiments indicates that the local self-energy and polarization contributions are overestimated in $GW+EDMFT$ relative to the nonlocal ones. As was discussed in Ref. [24], for weakly correlated materials with strong nonlocal screening, corrections beyond the RPA-type diagrams would be needed for the nonlocal part. The replacement of the local polarization by the EDMFT result, but the restriction of the nonlocal polarization

to a simple bubble, produces a mismatch between local and nonlocal screening effects and an incorrect estimation of the interaction. In the case of one-shot GW , the local and nonlocal polarizations are treated on equal footing, and the estimated T_c is improved accordingly.

The T_c is substantially different when only the self-energies and polarizations of the t_{2g} orbitals are corrected with the local quantities from EDFMT within the multiter $GW+EDMFT$ formalism, which produces results that are more similar to one-shot GW and $scGW$. This indicates two things: First that local corrections to the (almost empty) d orbitals are of minor importance in this material for the calculation of W and the description of the pressure dependence of the critical temperature, and second that the effects of treating the s and p states with the local EDMFT corrections is primarily responsible for the overestimation of T_c in $GW+EDMFT$. This agrees with the previous discussion on the importance of not adding the full local contributions to states whose screening is not well described by a bubble approximation to the nonlocal diagrams.

In contrast with the very sharp T_c valley found by Wu *et al.* [10] where the maxima on the two sides roughly coincide, we observe a more shallow structure with a significantly lower T_c on the low-pressure side of the valley for all methods tested. This is in agreement with the available experimental data which show a valley structure. The location of the valley is shifted to too high pressures by a few GPa compared with experiment, in agreement with Ref. [10]. Since the valley is located around the same pressure ($P \approx 20$ GPa) for all methods, this position is determined by the underlying DFT calculation and apparently is reasonably well described already at this level.

It is, furthermore, worth pointing out a second change to the $P-T_c$ curves. In the case of $GW+EDMFT$, the modifications are less trivial compared with the rigidly shifted G^0W^0 , $scGW$, and multiter $GW+EDMFT$ curves as becomes clear from Fig. 7. The most notable difference is an increase in the separation between the valley minimum and the T_c maximum ($\Delta T_c^{\text{peak}} \approx 3.5$ K) on the inclusion of the EDMFT self-energy and polarization. This behavior is consistent with the experimental data of Guo *et al.* [7] (the maximum, however, is located ~ 5 GPa too low in our calculations). In addition, at higher pressures, the T_c curve starts to deviate from the monotonic decline predicted by the other methods. A more thorough discussion on the changes to the valley and high-pressure dependence observed will be presented in the next section.

One may wonder if these deviations observed only in the $GW+EDMFT$ scheme are indicative of some nontrivial correlation effects not properly captured within the current SCDFT formalism, or if they merely represent an artifact of a method that is not suitable for treating a weakly correlated system such as simple cubic phosphorus, as discussed previously. To explore this question we have extended the SCDFT formalism to also take into account correlation-induced modifications of the DFT one-particle energies by replacing them with quasi-particle energies. This approach goes beyond a treatment of correlations through the screened interaction W only and will be described in the next section.

E. Quasiparticle correction

In the simulations so far, electronic correlation effects entered through the screened interaction W , while the phononic contribution and the band structure were taken from the original DFT calculation. Here we explore two more consistent schemes without fundamentally changing the formalism. Specifically, we will update the band structure and DOS in (i) the electronic contribution only by replacing the DFT one-particle energies and DOS by the quasiparticle energies obtained from the solution of the quasiparticle equation and (ii) by also approximately taking into account this change in the phononic kernel.

Since the solution of the quasiparticle equation requires knowledge of the frequency dependence of the self-energy, we use in the following calculations the G^0W^0 quasiparticle energies. These can be obtained without analytical continuation of $\Sigma(i\omega_n)$ to the real axis (the real-axis data are directly available from SPEX).

The quasiparticle energies $\varepsilon_{nk}^{\text{QP}}$ are calculated as the solution of the equation

$$\varepsilon_{nk}^{\text{QP}} = \varepsilon_{nk}^{\text{DFT}} + \Sigma_{nk}(\varepsilon_{nk}^{\text{QP}}) - V_{nk}^{\text{XC}} \quad (25)$$

and define the DOS $N^{\text{QP}}(\varepsilon)$. In scheme (i), these are then substituted for ε_{nk} and $N(\varepsilon)$ in Eqs. (19), (23), and (24). In scheme (ii), we additionally replace the one-particle energies in the Fermi surface integration in the calculation of α^2F [Eq. (7)] while keeping the electron-phonon coupling constants from DFT. For a fully consistent calculation, $g_{\lambda\mathbf{q}}^{nk,n'\mathbf{k}'}$ would also need to be recalculated. This could be done within the recently developed GW perturbation theory ($GWPT$) [51] where, in a manner similar to Eq. (25), the effects of the electronic self-energy correct the DFT V_{nk}^{XC} also in the calculation of the electron-phonon coupling constants $g_{\lambda\mathbf{q}}^{nk,n'\mathbf{k}'}$. Such a treatment, however, goes beyond the scope of the present study.

Applying the procedures (i) and (ii) to one-shot GW , we obtain in both cases a reduction in T_c so that the theoretical results are in reasonable agreement with most of the available experiments; see Fig. 8 (and Fig. 1 for additional experimental results). In addition to a rigid shift to an overall improved T_c , we note that the quasiparticle correction has an additional nontrivial effect on the pressure dependence. Method (i) produces a small upward shift in the high-pressure region (orange curve) compared with one-shot GW (blue curve), while the valley remains mostly unaffected. Strikingly, when the phononic contribution is also corrected in method (ii), the valley up to the peak maximum again remains approximately unaffected, while the high-pressure critical temperatures above 30 GPa are significantly pushed up compared with the low-pressure region (green curve). The relative shift increases with pressure, and the resulting pressure dependence becomes similar to the almost constant T_c found in some of the experiments. For a simpler comparison of the pressure dependence, we show the P - T_c curves shifted with respect to the valley minimum in Fig. 9 and compare them with the experimental data from Guo *et al.* [7] who observed a valley-ridge structure of the critical temperature.

Finally we also remark on what happens if the quasiparticle correction is applied to methods other than G^0W^0 .

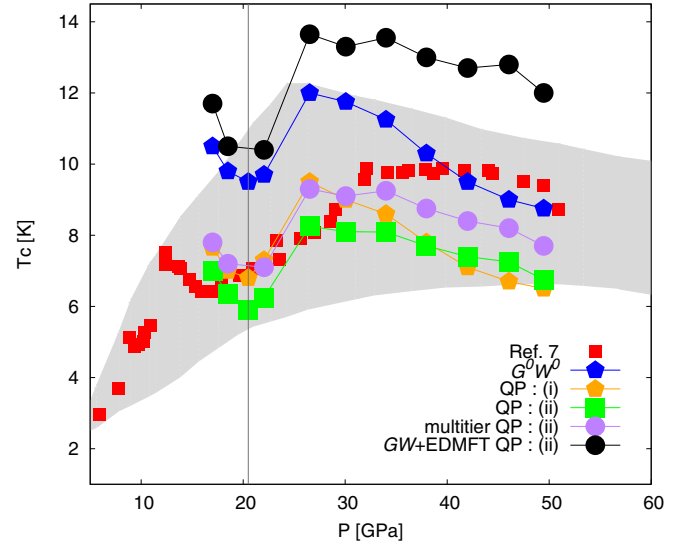


FIG. 8. Correction to the pressure dependence of the theoretically calculated critical temperature T_c for G^0W^0 from the quasiparticle band structure. The two methods (i) and (ii) described in the text are compared with the experimental data from Ref. [7] and the original G^0W^0 results. Also the (multiter) GW +EDMFT result corrected with the G^0W^0 quasiparticle energies is shown for comparison. To the left of the vertical line we observe a structural instability in our phonon calculations. The full frequency dependence of the electronic contributions has been considered here.

For this discussion, we focus on the most advanced method considered in this work, GW +EDMFT. Since GW +EDMFT calculations are performed on the Matsubara axis, we do not have direct access to the $\Sigma(\omega)$ needed for the solution of Eq. (25), and a numerical analytical continuation would be required. Here we limit ourselves to just correcting the band structure and DOS in methods (i) and (ii) with the

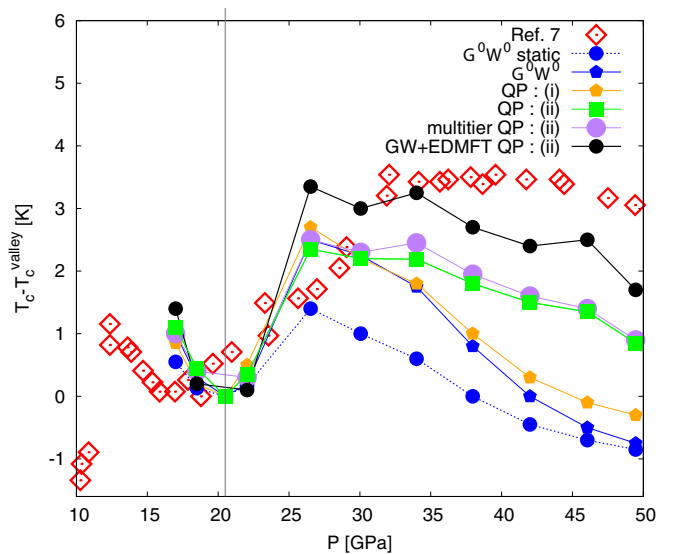


FIG. 9. Calculated critical temperature T_c shifted with respect to the valley minimum for the various G^0W^0 calculations and the (multiter) GW +EDMFT results corrected with the G^0W^0 quasiparticle energies compared with the experimental data reported in Ref. [7].

$\varepsilon_{nk}^{\text{QP}}$ obtained from one-shot GW which are known exactly. In the SCDFT scheme, this change corresponds to using a G^0W^0 quasiparticle band structure instead of that of DFT while ignoring further corrections to the quasiparticle energies from the EDMFT self-consistency cycle in the model space. Since the bare propagators $G_{\mathbf{k}}^0$ of the model contain a G^0W^0 -type self-energy correction, we believe that this is more consistent than the use of the DFT bands. The incorporation of GW +EDMFT-derived quasiparticle energies into SCDFT will be left for future work.

Before describing the results we want to repeat that GW +EDMFT is arguably not the best choice for a weakly correlated material like black phosphorus. Nevertheless, the effects of the quasiparticle correction are once again remarkable. As seen by comparing Figs. 8 and 7 (black curves), the severe overestimation of T_c in the original GW +EDMFT is to a large extent corrected, with the theoretical predictions becoming closer to the experimental results, now comparable in magnitude to the predictions from the uncorrected multitier calculations (green curve in Fig. 7). This indicates either that the quasiparticle approach somehow corrects the overestimation of T_c coming from the inconsistent treatment of local and nonlocal correlations in the s and p subspaces or (more likely) that the overestimation of T_c is linked primarily to an inconsistency between the screened interaction W and the band energies used in the SCDFT calculation. In the latter case, the lowest-order description of the nonlocal screening would then merely be responsible for the remaining modest overestimation of T_c .

The most interesting effect on the GW +EDMFT results is, however, as in the case of G^0W^0 , the formation of a ridgelike structure at higher pressures. While the structure of the valley remains mostly unchanged, ΔT_c^{peak} retains its good agreement with the experiments of Guo *et al.*, as demonstrated in Fig. 9. The same quasiparticle correction applied to the multitier GW +EDMFT scheme is shown as well with a mostly rigid shift from the G^0W^0 result, as in the uncorrected case. The same ridgelike high-pressure dependence is observed, and the shift to higher T_c brings the theoretically calculated critical temperatures closer to the experimental reference values available in this pressure range.

The differences between the multitier and the GW +EDMFT results support the previous conclusion about the origin of the remaining overestimation of T_c in the GW +EDMFT framework coming from the incorrect description of the nonlocal screening in this class of materials. On the other hand, the effects of the quasiparticle corrections also indicate that a better starting point than the initial DFT (GGA) calculation or more accurate quasiparticle energies is required for a quantitatively accurate description.

IV. SUMMARY AND CONCLUSIONS

We have tested the reliability and predictive power of the SCDFT scheme and showed how it can be combined with the dynamically screened interactions from state-of-the-art many-body methods. By systematically studying simple cubic phosphorus under pressure, we have tested the strengths and weaknesses of different schemes for this type of weakly

correlated material. Specifically, by adding the dynamic part of the electronic kernel and limiting the effects of correlations to only W , we do not observe any formation of a ridge in the P - T_c dependence at high pressures, as speculated in Ref. [10]. Instead, a rigid shift to higher T_c is found, bringing the theoretical values closer to the experimental ones. In addition to demonstrating the importance of using the full frequency dependence of the interaction to obtain meaningful estimates of the critical temperature for all the methods considered, this suggests that the peculiar pressure dependence of T_c in the high-pressure region is not only of plasmonic origin. We further found that the formation of a T_c valley in the simple cubic phase is predicted a few GPa too high compared with the experiments, independent of the method. This feature is, therefore, a result of the underlying DFT calculations and the Lifshitz transitions observed in this region, in agreement with the previous work by Wu *et al.* [10] based on the McMillan equation.

Without corrections to the SCDFT formalism from correlations beyond W , the theoretical methods related to one-shot GW provide the overall best agreement of T_c with the available experimental data, confirming that the resummation of a subclass of diagrams in $scGW$ also worsens the accuracy for this material-dependent property. Similarly, in the case of GW +EDMFT, the omission of higher-order nonlocal polarization diagrams together with the more exact treatment of local contributions does not work well (specifically when applied to the s and p orbitals), in agreement with previous discussions related to the application of GW +EDMFT to weakly correlated materials [24].

We further observed that with increasing complexity of the treatment of correlations, the pressure dependence of T_c is changing from a monotonous decay (with increasing pressure) toward a valley-ridge structure, in good agreement with recent experiments predicting such a nontrivial structure [7]. Modifications in the treatment of the phononic contribution have significant effects on the high-pressure (25–50 GPa) P - T_c curve, whereas the low-pressure region remains mostly unaffected. We have considered here an *ad-hoc* modification of the phononic kernel, which corresponds to replacing the DFT band structure with the quasiparticle energies from G^0W^0 and partially recalculating the phonons with these modified bands. This indicates the importance of the initial starting point for the phonon calculation. $GWPT$ [51] could give an improved description, or the use of alternative phononic kernels, such as recently proposed in Ref. [52], may provide a viable route.

Although it is questionable if GW +EDMFT is a suitable method for black phosphorus, we have demonstrated a relative success in the description of the high-pressure dependence of T_c , especially in combination with the quasiparticle correction to the phonons. Due to the dependence of the theoretical results on the method used to obtain the electronic kernel, we speculate that the combination of GW +EDMFT and SCDFT could work well for more strongly correlated systems, where GW +EDMFT should provide a superior description of the fully screened electron-electron interaction compared with the other methods considered [23,24,53–55]. This point will be investigated in future works. To properly capture the renormalized momentum-dependent spectral function also within the SCDFT formalism, some type of quasiparticle correction

would, however, have to be implemented in the calculation of the electronic and phononic kernels. For the phononic part, an improved starting point could be obtained from a DFT+DMFT calculation of the phonons [56,57] or using DFT+ U [58,59].

To summarize, our results show that many-body calculations of the screened interaction W in combination with the parameter-free SCDFT formalism for calculating T_c provides a framework that is capable of predicting the correct range of T_c values in the simple cubic phase of black phosphorus. While the frequency dependence of the interaction is important for obtaining realistic T_c values, it is not solely responsible for the peculiar pressure versus T_c dependence that has been observed in experiments. Instead, our results indicate that it is important to use an improved phononic contribution, which goes beyond the common DFT-based kernel. To clarify whether or not quasiparticle corrections are sufficient for an accurate prediction of the P - T_c diagram, more systematic and rigorous calculations and additional accurate experimental reference data would be needed.

ACKNOWLEDGMENTS

The calculations have been performed on the Beo05 cluster at the University of Fribourg. This work was supported by ERC Consolidator Grant No. 724103 and by the Swiss National Science Foundation via NCCR Marvel and Grant No. 200021-196966.

APPENDIX: T_c FROM THE MCMILLAN FORMULA

The superconducting critical temperature can also be estimated from the Allen-Dynes modified McMillan formula [13,14]. In Fig. 10 this estimate is compared with the T_c calculated within SCDFT using the fully frequency-dependent electronic kernel from one-shot GW . The effective interaction $\mu^* = 0.10$ was chosen such that the minima coincide in the valley region. The electron-phonon coupling constants λ , ω_{in} , and ω_{rms} used in the McMillan formula are listed in Table I. To further highlight the importance of the details of the electronic structure and its effect on the effective interaction for simple cubic phosphorus under pressure, we also include the μ^*

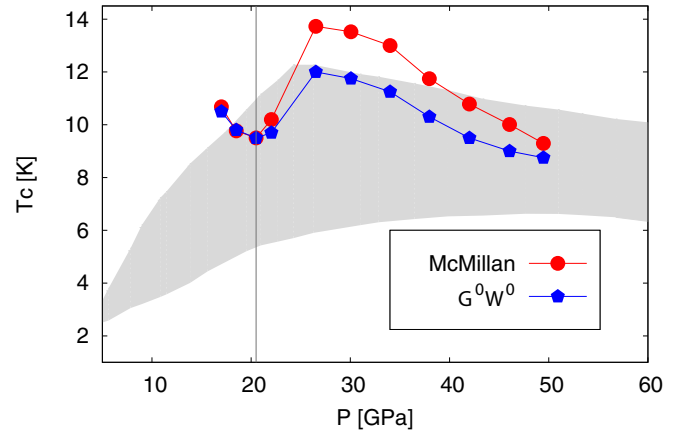


FIG. 10. Theoretically calculated critical temperature T_c from the McMillan formula (with $\mu^* = 0.10$) and from SCDFT (with the frequency-dependent electronic kernel from one-shot GW) as a function of pressure P compared with the experimental results (gray shading). To the left of the vertical line we observe a structural instability in our phonon calculations.

values corresponding to the T_c obtained from SCDFT. These values show a $\sim 16\%$ difference between the valley and the peak maximum.

TABLE I. Pressure dependence of λ , ω_{in} , and ω_{rms} . Also shown are the estimates of the effective interaction μ^* based on the T_c values calculated with SCDFT and the fully frequency-dependent interaction kernel from G^0W^0 .

P (GPa)	λ	ω_{in} (K)	ω_{rms} (K)	μ^* (G^0W^0)
17.0	0.631	388	416	0.101
18.5	0.606	400	426	0.098
20.5	0.595	411	436	0.099
22.0	0.607	414	440	0.104
26.5	0.684	401	440	0.114
30.1	0.667	423	460	0.114
34.0	0.647	440	477	0.114
38.0	0.619	451	491	0.111
42.0	0.598	458	503	0.110
46.0	0.582	464	514	0.108
49.5	0.566	470	524	0.104

[1] T. Kikegawa and H. Iwasaki, *Acta Crystallogr. Sect. B: Struct. Sci.* **39**, 158 (1983).
[2] Y. Akahama, M. Kobayashi, and H. Kawamura, *Phys. Rev. B* **59**, 8520 (1999).
[3] H. Kawamura, I. Shirotni, and K. Tachikawa, *Solid State Commun.* **49**, 879 (1984).
[4] H. Kawamura, I. Shirotni, and K. Tachikawa, *Solid State Commun.* **54**, 775 (1985).
[5] I. Shirotni, H. Kawamura, K. Tsuji, K. Tsuburaya, O. Shimomura, and K. Tachikawa, *Bull. Chem. Soc. Jpn.* **61**, 211 (1988).

[6] J. Wittig, B. Bireckoven, and T. Weidlich, *Solid State Physics Under Pressure*, edited by S. Minomura (KTK Scientific Publishers, Tokyo, 1985), p. 217.
[7] J. Guo, H. Wang, F. von Rohr, W. Yi, Y. Zhou, Z. Wang, S. Cai, S. Zhang, X. Li, Y. Li, J. Liu, K. Yang, A. Li, S. Jiang, Q. Wu, T. Xiang, R. J. Cava, and L. Sun, *Phys. Rev. B* **96**, 224513 (2017).
[8] M. Karuzawa, M. Ishizuka, and S. Endo, *J. Phys.: Condens. Matter* **14**, 10759 (2002).
[9] J. A. Flores-Livas, A. Sanna, A. P. Drozdov, L. Boeri, G. Profeta, M. Eremets, and S. Goedecker, *Phys. Rev. Materials* **1**, 024802 (2017).

- [10] X. Wu, H. O. Jeschke, D. Di Sante, F. O. von Rohr, R. J. Cava, and R. Thomale, *Phys. Rev. Mater.* **2**, 034802 (2018).
- [11] P. Hohenberg and W. Kohn, *Phys. Rev.* **136**, B864 (1964).
- [12] W. Kohn and L. J. Sham, *Phys. Rev.* **140**, A1133 (1965).
- [13] W. L. McMillan, *Phys. Rev.* **167**, 331 (1968).
- [14] P. B. Allen and R. C. Dynes, *Phys. Rev. B* **12**, 905 (1975).
- [15] L. N. Oliveira, E. K. U. Gross, and W. Kohn, *Phys. Rev. Lett.* **60**, 2430 (1988).
- [16] M. Lüders, M. A. L. Marques, N. N. Lathiotakis, A. Floris, G. Profeta, L. Fast, A. Continenza, S. Massidda, and E. K. U. Gross, *Phys. Rev. B* **72**, 024545 (2005).
- [17] M. A. L. Marques, M. Lüders, N. N. Lathiotakis, G. Profeta, A. Floris, L. Fast, A. Continenza, E. K. U. Gross, and S. Massidda, *Phys. Rev. B* **72**, 024546 (2005).
- [18] D. Pines, *Elementary Excitations in Solids* (W. A. Benjamin, New York), 1963.
- [19] R. Akashi and R. Arita, *Phys. Rev. Lett.* **111**, 057006 (2013).
- [20] L. Hedin, *Phys. Rev.* **139**, A796 (1965).
- [21] S. Biermann, F. Aryasetiawan, and A. Georges, *Phys. Rev. Lett.* **90**, 086402 (2003).
- [22] T. Ayrál, S. Biermann, and P. Werner, *Phys. Rev. B* **87**, 125149 (2013).
- [23] L. Boehnke, F. Nilsson, F. Aryasetiawan, and P. Werner, *Phys. Rev. B* **94**, 201106(R) (2016).
- [24] F. Nilsson, L. Boehnke, P. Werner, and F. Aryasetiawan, *Phys. Rev. Mater.* **1**, 043803 (2017).
- [25] J. P. Perdew, K. Burke, and M. Ernzerhof, *Phys. Rev. Lett.* **77**, 3865 (1996).
- [26] The FLEUR group, The FLEUR project, <http://www.flapw.de>.
- [27] M. Aoki, N. Suzuki, and K. Motizuki, *J. Phys. Soc. Jpn.* **56**, 3253 (1987).
- [28] M. Rajagopalan, M. Alouani, and N. E. Christensen, *J. Low Temp. Phys.* **75**, 1 (1989).
- [29] K. T. Chan, B. D. Malone, and M. L. Cohen, *Phys. Rev. B* **88**, 064517 (2013).
- [30] P. Vinet, J. Ferrante, J. R. Smith, and J. H. Rose, *J. Phys. C* **19**, L467 (1986).
- [31] N. Marzari and D. Vanderbilt, *Phys. Rev. B* **56**, 12847 (1997).
- [32] A. A. Mostofi, J. R. Yates, Y.-S. Lee, I. Souza, D. Vanderbilt, and N. Marzari, *Comput. Phys. Commun.* **178**, 685 (2008).
- [33] F. Aryasetiawan, M. Imada, A. Georges, G. Kotliar, S. Biermann, and A. I. Lichtenstein, *Phys. Rev. B* **70**, 195104 (2004).
- [34] M. van Schilfgaarde, T. Kotani, and S. Faleev, *Phys. Rev. Lett.* **96**, 226402 (2006).
- [35] To disentangle the seven bands in the low-energy model, we used an outer window up to 40 eV and an inner window between $-5:5$ eV in the Wannierization.
- [36] C. Friedrich, S. Blügel, and A. Schindlmayr, *Phys. Rev. B* **81**, 125102 (2010).
- [37] W. Metzner and D. Vollhardt, *Phys. Rev. Lett.* **62**, 324 (1989).
- [38] A. Georges, G. Kotliar, W. Krauth, and M. J. Rozenberg, *Rev. Mod. Phys.* **68**, 13 (1996).
- [39] P. Sun and G. Kotliar, *Phys. Rev. B* **66**, 085120 (2002).
- [40] P. B. Allen, *Phys. Rev. B* **6**, 2577 (1972).
- [41] The ELK code, <http://elk.sourceforge.net/>.
- [42] K. Tsutsumi, Y. Hizume, M. Kawamura, R. Akashi, and S. Tsuneyuki, *Phys. Rev. B* **102**, 214515 (2020).
- [43] A. Zangwill and P. Soven, *Phys. Rev. A* **21**, 1561 (1980).
- [44] E. K. U. Gross and W. Kohn, *Phys. Rev. Lett.* **55**, 2850 (1985).
- [45] R. Akashi, K. Nakamura, R. Arita, and M. Imada, *Phys. Rev. B* **86**, 054513 (2012).
- [46] O. Jepsen and O. Anderson, *Solid State Commun.* **9**, 1763 (1971).
- [47] G. Lehmann and M. Taut, *Phys. Status Solidi B* **54**, 469 (1972).
- [48] R. Akashi, M. Kawamura, S. Tsuneyuki, Y. Nomura, and R. Arita, *Phys. Rev. B* **91**, 224513 (2015).
- [49] M. Kawamura, R. Akashi, and S. Tsuneyuki, *Phys. Rev. B* **95**, 054506 (2017).
- [50] B. Holm and U. von Barth, *Phys. Rev. B* **57**, 2108 (1998).
- [51] Z. Li, G. Antonius, M. Wu, F. H. da Jornada, and S. G. Louie, *Phys. Rev. Lett.* **122**, 186402 (2019).
- [52] A. Sanna, C. Pellegrini, and E. K. U. Gross, *Phys. Rev. Lett.* **125**, 057001 (2020).
- [53] F. Petocchi, F. Nilsson, F. Aryasetiawan, and P. Werner, *Phys. Rev. Res.* **2**, 013191 (2020).
- [54] F. Petocchi, V. Christiansson, F. Nilsson, F. Aryasetiawan, and P. Werner, *Phys. Rev. X* **10**, 041047 (2020).
- [55] F. Petocchi, V. Christiansson, and P. Werner, *Phys. Rev. B* **104**, 195146 (2021).
- [56] S. Y. Savrasov and G. Kotliar, *Phys. Rev. Lett.* **90**, 056401 (2003).
- [57] C. P. Koçer, K. Haule, G. L. Pascut, and B. Monserrat, *Phys. Rev. B* **102**, 245104 (2020).
- [58] A. Floris, S. de Gironcoli, E. K. U. Gross, and M. Cococcioni, *Phys. Rev. B* **84**, 161102(R) (2011).
- [59] J.-J. Zhou, J. Park, I. Timrov, A. Floris, M. Cococcioni, N. Marzari, and M. Bernardi, *Phys. Rev. Lett.* **127**, 126404 (2021).